Cell Reports
Physical Science

CellPress
OPEN ACCESS

Report

Ultrasensitive and highly specific detection of iodine ions using zirconium (IV)-enhanced oxidation

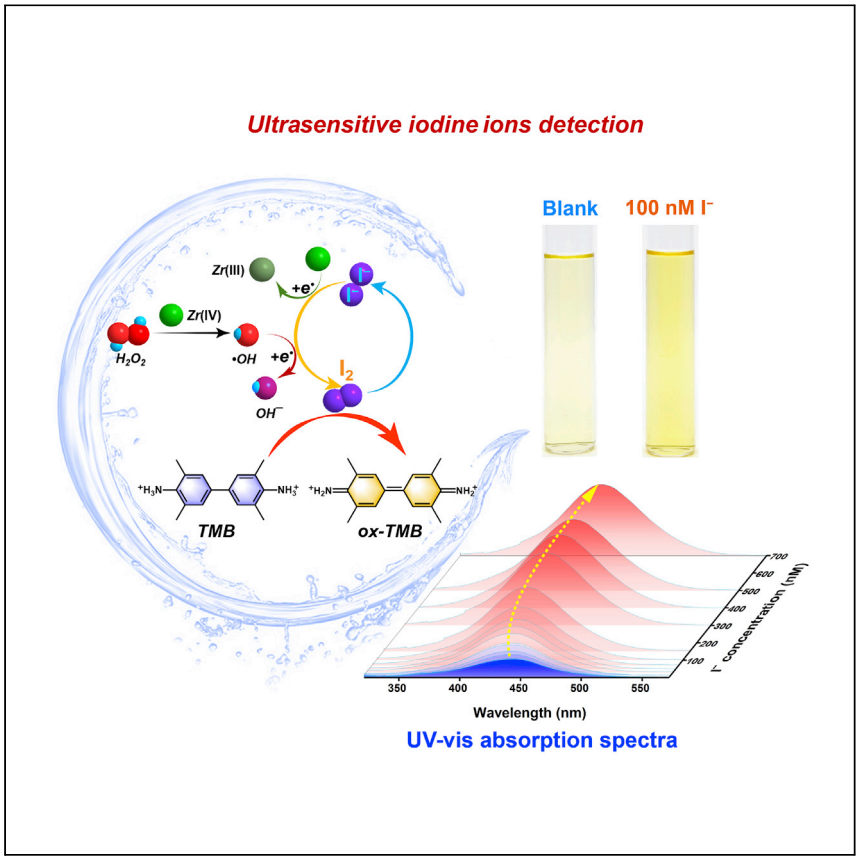

Feng et al. report the high-sensitivity detection of I^- enhanced by Zr(IV). Zr(IV) can directly and indirectly oxidize I^- by promoting the generation of •OH to obtain I_2. This results in the oxidization of 3,3′,5,5′-tetramethylbenzidine with detectable signal and ultrahigh I^- detection sensitivity.

Tiantian Feng, Yihui Yuan, Xuran Chen, ..., Roberto Scaffaro, Biao He, Ning Wang

yuanyh@hainau.edu.cn (Y.Y.)
wangn02@foxmail.com (N.W.)

Highlights

Zr(IV) enhances the detection of I^- by boosting the generation of I_2

Ultrasensitive detection of I^- with high specificity and high reliability

The detection method is applicable in diverse environments

Feng et al., Cell Reports Physical Science 3, 101143
November 16, 2022
https://doi.org/10.1016/j.xcrp.2022.101143

Cell Reports
Physical Science

CellPress
OPEN ACCESS

Report

Ultrasensitive and highly specific detection of iodine ions using zirconium (IV)-enhanced oxidation

Tiantian Feng,[1] Yihui Yuan,[1,*] Xuran Chen,[1] Shilei Zhao,[1] Meng Cao,[1] Lijuan Feng,[1] Se Shi,[1] Hui Wang,[1] Tao Liu,[1] Alexander Pud,[2] Li Han,[3] Roberto Scaffaro,[4] Biao He,[5] and Ning Wang[1,6,*]

SUMMARY

Nuclear energy has significantly promoted the development of human society. However, nuclear pollution caused by nuclear accidents can lead to significant hazards to the environment and human health. As a major radioactive product, radioactive iodine (mainly existing as I^-) detection has attracted significant attentions. In this study, zirconium(IV) is used to enhance the oxidation of environmental I^- to form I_2. Subsequently, the generated I_2 oxidizes the chemical chromogenic substrate 3,3′,5,5′-tetramethylbenzidine, which is used for I^- detection and realizes an ultralow limit of detection (LoD) of 0.176 nM. The LoD of our method, to the best of our knowledge, is the lowest among those of the available chemical methods for I^- detection. Furthermore, our detection method also shows high specificity and reliability, making it a promising technique for detecting I^- in practical environments.

INTRODUCTION

Nuclear power supplies approximately 13% of the global electricity consumption and will continue to play an important role in the development of human society.[1–9] However, radioactive elements produced by nuclear fission seriously threaten human society and environmental safety.[10–15] Iodide (I^-) is the dominant form of iodine among I^-, IO_3^-, I_2, HOI, and organic iodine,[16,17] and it is one of the most problematic radionuclides generated during the nuclear fuel cycle owing to its high radioactivity and extremely high solubility and mobility.[18,19] The nuclear accident of the Fukushima Daiichi nuclear power plant in 2011 caused the leakage of radioactive iodine, including ^{129}I and ^{131}I, mainly in the form of I^-.[20] Furthermore, the Japanese government plans to discharge nuclear wastewater in 2023, which will cause more serious harm to the environment.[21,22] Therefore, the detection of environmental I^- is of vital importance.

Recently, various methods have been used for the quantification of I^-, including high-performance liquid chromatography,[23] capillary electrophoresis,[24] mass spectrometry,[25] and Raman scattering spectrometry.[26] However, these methods usually rely on expensive equipment and complicated pre-operation processes, making them unsuitable for practical applications.[27–29] Hence, chemical detection methods are designed based on the interaction between I^- and chemical chelates,[30–33] which can generate detection signals, including optical signals and electrochemical signals.[34–36] However, these methods depend on the recognition of I^- by chemical chelates, which can be interfered by the coexisting ions.[37] The 3,3′,5,5′-tetramethylbenzidine (TMB) is a chemical chromogenic substrate used in

[1]State Key Laboratory of Marine Resource Utilization in South China Sea, Hainan University, Haikou 570228, P.R. China

[2]V.P. Kukhar Institute of Bioorganic Chemistry and Petrochemistry, National Academy of Sciences of Ukraine, 50 Kharkivske Shose, 02160 Kyiv, Ukraine

[3]Department of Energy Conversion and Storage, Technical University of Denmark, Elektroevej Building 375, 2800 Kgs. Lyngby, Denmark

[4]Department of Engineering, University of Palermo, Viale delle Scienze, Ed. 6, 90128 Palermo, Italy

[5]Institute for Materials, Ruhr-Universität Bochum, Universitätsstraße 150, 44801 Bochum, Germany

[6]Lead contact

*Correspondence: yuanyh@hainau.edu.cn (Y.Y.), wangn02@foxmail.com (N.W.)

https://doi.org/10.1016/j.xcrp.2022.101143

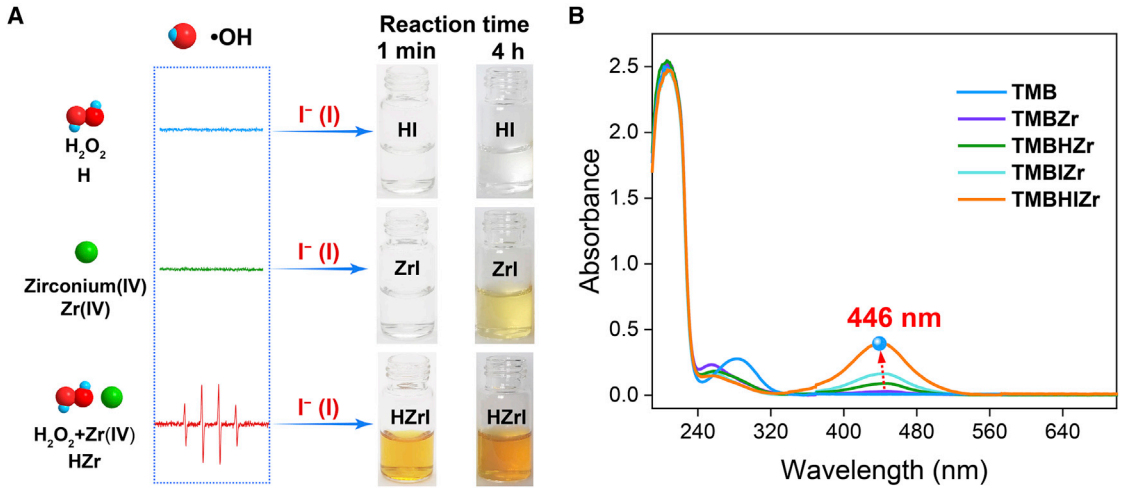

Figure 1. Ability of Zr(IV) in enhancing the oxidization of I^- and TMB

(A) ESR spectra of •OH radicals from the solutions containing H_2O_2 (denoted as H), Zr(IV), and the coexistence of H_2O_2 and Zr(IV) (denoted as HZr). The photographs of the corresponding solutions treated by I^- for 1 min and 4 h are shown.

(B) Absorbance spectra of TMB, TMBZr, TMBHZr, TMBIZr, and TMBHIZr after the reaction time of 12 h.

the development of colorimetric detection methods because of its high sensitivity, good color purity for colored products, and high stability of its oxidation products.[38,39] TMB can be oxidized to a cation radical TMB^+ or diimine TMB^{2+}. The TMB^{2+} can be detected using ultraviolet-visible (UV-vis) spectrophotometer at the absorbance wavelength of 450 nm.[40] In the presence of H_2O_2, I^- can trigger the oxidation of TMB by forming I_2, which has been applied for detection of I^-.[41] However, owing to insufficient oxidation of I^-, this detection method only realizes a low detection sensitivity and cannot fulfill practical demands. Therefore, strategies with enhanced detection sensitivity, specificity, and operation convenience are urgently required for the practical detection of I^-.

Zirconium(IV), denoted as Zr(IV), is a Lewis acid metal center with high chemical stability and outstanding catalytic activity.[42,43] Different types of Zr(IV)-containing materials, including Zr-metal-organic frameworks (MOFs),[44,45] ZrO_2,[46] basic zirconium carbonate,[47] zirconium phosphate catalysts,[48] and $Zr(OH)_4$, have been used as catalysts.[49] However, the application of Zr(IV) in enhancing the detection sensitivity of I^- has not been reported yet. In this study, Zr(IV), in the form of $ZrOCl_2$,[50,51] is obtained by dissolving $ZrCl_4$ in deionized water and is used to enhance the ability of TMB to detect I^- in the presence of H_2O_2. Zr(IV) enhances the oxidation of I^- to I_2 and triggers the transformation of H_2O_2 to hydroxyl radicals (•OH), which also oxidize I^- to I_2. Subsequently, the oxidized iodine oxidizes TMB to obtain oxidized TMB (*ox*-TMB) with a yellow color, which is used to detect I^-. Owing to the enhanced transformation of I^- to I_2 by Zr(IV), ultrahigh sensitivity of I^- detection in diverse aqueous environments is successfully realized.

RESULTS AND DISCUSSION

Mechanism of enhanced I^- oxidation by Zr(IV)

The mechanism of Zr(IV) to enhance the oxidation of I^- was analyzed. Electron spin resonance (ESR) analysis showed that the coexistence of Zr(IV) with H_2O_2 caused the generation of •OH, indicating that Zr(IV) exhibited peroxidase-like activity to trigger the homolytic splitting of H_2O_2 into •OH (Figure 1A). After the addition of I^-, the mixture of Zr(IV) and H_2O_2 turned orange due to the oxidation of I^- by •OH to

form I_2. ESR analysis of the solution after the addition of I^- showed that the signal of the •OH radical was significantly decreased, proving that •OH was utilized in oxidizing I^- to I_2 (Figure S1). Furthermore, the ability of Zr(IV) alone to trigger the formation of I_2 was determined by analyzing the absorbance spectra of the I^- solutions treated with Zr(IV) and both H_2O_2 and Zr(IV). The results showed that I_3^- generated by the interaction between I_2 and I^- was detected in all samples containing Zr(IV), confirming the ability of Zr(IV) to promote the oxidation of I^- to I_2 (Figure S2). X-ray photoelectron spectroscopy (XPS) analysis of the mixture containing Zr(IV) and I^- also showed that Zr(IV) was reduced to Zr(III), existing in its stable form ZrO^+,[52] by obtaining electrons from I^- (Figure S3). These results reveal that Zr(IV) enhances the oxidation of I^- by combining two approaches, including the direct oxidation of I^- and the indirect oxidation of I^- by boosting the generation of •OH.

Enhanced oxidation of TMB by Zr(IV)

The ability of Zr(IV) to enhance the oxidation of TMB was determined by monitoring the characteristic absorbance peak of *ox*-TMB at approximately 446 nm. The effects of H_2O_2, I^-, and Zr(IV) on the oxidation of TMB were determined. Upon adding Zr(IV) to the TMB solution, indicated as TMBZr, a nearly negligible peak at 446 nm, corresponding to the *ox*-TMB, was observed (Figure S4). This weak peak indicates that Zr(IV) only possesses a low oxidation ability to TMB. Upon the addition of H_2O_2 or I^- to the TMB solution, indicated as TMBH and TMBI, respectively, there was no observable peak at 446 nm. However, the addition of Zr(IV) with either H_2O_2 or I^- to TMB, denoted as TMBHZr or TMBIZr, respectively, resulted in strong peaks at approximately 446 nm (Figure 1B). These results indicate that Zr(IV) can oxidize TMB in cooperation with H_2O_2 or I^-. The coexistence of all four substances, denoted as TMBHIZr, led to the most significant change of the absorbance at 446 nm, which is even distinguishable by the naked eye, indicating that the oxidation of TMB can reach a maximum only by the coexistence of I^-, Zr(IV), and H_2O_2.

Mechanism of enhanced TMB oxidation by Zr(IV)

The oxidation mechanism of TMB by Zr(IV) was further analyzed. The Fourier-transform infrared (FTIR) spectroscopy analysis showed that, compared with the spectrum of TMB, the peak corresponding to the C=N bond (1,566 cm^{-1}) was detected, and the peak corresponding to the C–N bond (1,095 cm^{-1}) was weakened, in the spectrum of TMBHIZr, which was because that C–NH_3^+ group in TMB was oxidized into the C=NH_2^+ group (Figure 2A). Furthermore, the peaks of the –NH_2 group (3,433 and 3,358 cm^{-1}), which were specific for TMB, were also detected in the spectrum of TMBHI, indicating that TMB was not completely oxidized in the TMBHI system (Figure S5). XPS analysis of the precipitate generated from TMBHIZr revealed an extremely low amount of Zr(IV) and a high amount of iodine (Figure 2B). The results of scanning electron microscopy (SEM) together with energy-dispersive spectroscopy (EDS) further proved the results of XPS analysis (Figure 2C).[53] The N *1s* spectrum of TMB possessed two peaks at 401.6 and 399.6 eV, which were assigned to the N–H and C–N groups, respectively (Figure S6). As for the coexistence of TMB with both Zr(IV) and H_2O_2, the two peaks corresponding to the =NH_2^+ (400.6 eV) and C=N (398.9 eV) groups were detected, which was attributed to the oxidized TMB. The ESR analysis showed, with the addition of Zr(IV), that the ESR intensity of TMBHIZr was much higher than that of TMBHI, demonstrating that Zr(IV) significantly promoted the oxidation of TMB (Figure 2D). The iodine species in TMBHI and TMBHIZr were determined using Raman spectroscopy. The result showed that peaks corresponding to I_3^- (104 cm^{-1}) and I_2 (212 cm^{-1}) were detected in TMBHIZr, attributing to the oxidation of I^- (Figure 2E). The oxidation of I^- by •OH and Zr(IV) produced I_2, which interacted with I^- in the mixture to form I_3^-. Compared

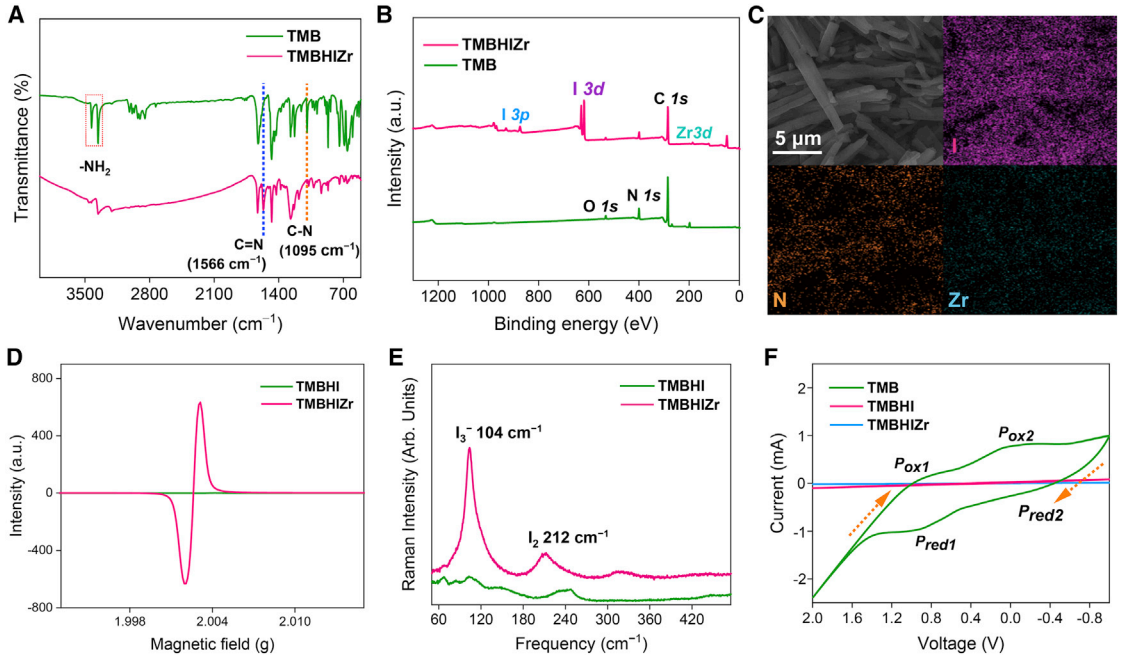

Figure 2. Mechanism of Zr(IV) in boosting the oxidation of TMB

(A) FTIR spectra of TMB and TMBHIZr.

(B) XPS spectra of TMB and TMBHIZr.

(C) SEM images and corresponding EDS elemental mapping of TMBHIZr.

(D) ESR spectrum of TMBHIZr and TMBHI.

(E) Raman spectra of TMBHI and TMBHIZr.

(F) Cyclic voltammograms of TMB, TMBHI, and TMBHIZr.

with these peaks in the spectrum of TMBHI, higher peak intensities were observed in the spectrum of TMBHIZr, which further proved the ability of Zr(IV) to promote the oxidation of I^- and subsequently facilitated the oxidation of TMB.

The oxidation of TMB was also analyzed by determining its electrooxidation behavior by means of cyclic voltammetry (Figure 2F). For TMB alone, two pairs of separated redox peaks, corresponding to the one-electron and two-electron oxidation stages of TMB, were detected.[54,55] The separated states of these two redox peaks indicated that these two oxidation steps can occur in a stepwise manner without overlap. However, these redox peaks disappeared in the cases of TMBHI and TMBHIZr, indicating that TMB in TMBHI and TMBHIZr maintained low redox activity under electrochemical conditions. The low redox activity of TMB in TMBHIZr was because that TMB has been completely oxidized into its two-electron oxidation product, which was the reason for its high chromogenic efficiency. Although TMB has been detected by FTIR in the TMBHI system, it was difficult to be further oxidized because of its low redox activity in TMBHI. This may be the reason for the low detection sensitivity of the previous method based on the oxidation of TMB by the coexistence of I^- and H_2O_2.[41]

Optimization of the detection system

To optimize the conditions for I^- detection, the effects of Zr(IV) concentration, pH, and salt concentration on the oxidation of TMB were analyzed by measuring the absorbance difference ΔA before and after the addition of I^- into the solution containing TMB, H_2O_2, and Zr(IV). The increase in Zr(IV) concentration led to the rise of ΔA, and the maximum ΔA was obtained with a Zr(IV) concentration of 1 mM (Figure S7). Furthermore, constant absorbance with or without the addition of I^- was observed in the

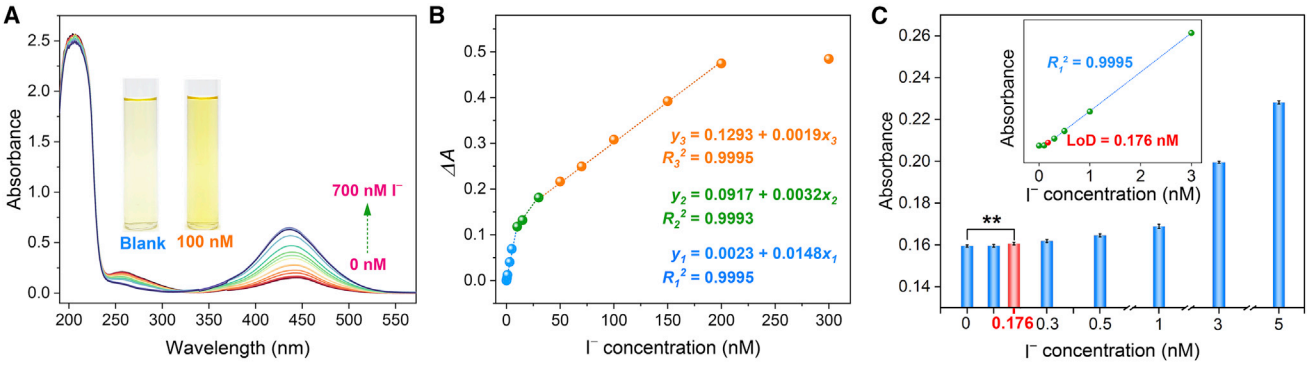

Figure 3. Performance of the proposed method in I^- detection

(A) UV-vis absorbance spectra of the mixtures of TMB, Zr(IV), and H_2O_2 containing different concentrations of I^-. The mixtures were left to react for 12 h. The colors of the mixture before and after adding I^- are shown in the inset.

(B) Linear relationships between ΔA and I^- concentrations in the range of 0–300 nM.

(C) Verification of the LoD for detecting I^-.

One-way ANOVA followed by Tukey's post hoc tests was used to perform the multiple comparisons among the absorbance value with different I^- concentrations. Data are presented as mean values ± SD from n = 5 independent experiments. **p < 0.01. All statistics were performed using IBM SPSS Statistics 24.0.

presence of 0.0125 mM TMB, 0.065 mM H_2O_2, and 1 mM Zr(IV) within the initial solution pH range of 4–10 (Figure S8). Thus, a broad range of initial pH values (from 4 to 10) was suitable for the detection of I^- using our method. Analysis of the reaction time for the oxidation of TMB after the addition of I^- showed that a stable ΔA was reached after 12 h of reaction (Figure S9). Thus, a reaction time of 12 h was selected for I^- detection. For salt concentrations lower than 300 μM, the mixture exhibited a stable absorbance both before and after the addition of I^-, indicating that salt concentrations lower than 300 μM were suitable for the detection of I^- using our method (Figure S10). Based on the above analysis, a system containing 0.0125 mM TMB, 0.065 mM H_2O_2, and 1 mM Zr(IV) was used for the detection of I^- in aqueous environments.

Validation of the detection method for I^-

To verify the performance of the constructed system in I^- detection, I^- was added to the optimal system containing TMB, H_2O_2, and Zr(IV) and left to react for 12 h. The intensity of the peak at approximately 446 nm increased gradually with the increase in I^- concentration (Figure 3A). Notably, with increasing I^- concentration, a blue shift of the peak was observed. This was due to the oxidation of TMB, leading to the transformation of the C–NH_3^+ group in TMB to the C=NH_2^+ group and causing a change in the conjugated system of the benzene ring in the molecule. The absorbance difference ΔA exhibited a linear relationship ($R^2 > 0.999$) with the concentration of I^- at 0.3–10, 10–30, and 30–200 nM (Figure 3B). Based on this relationship, the limit of detection (LoD) of this method was calculated to be 0.176 nM (0.022 μg L^{-1}) using the following formula: $3\sigma/k$,[56] where σ was obtained by conducting 20 repeated detections of the mixed solution without adding I^-. The absorbance of the solution containing 0.176 nM I^- was significantly different from that of the solution without I^-, confirming the ability of this method to detect I^- at concentrations as low as 0.176 nM and demonstrating the reliability of the calculated LoD (Figure 3C). Owing to the addition of Zr(IV), the LoD of the proposed method is approximately 2,200 times lower than that of the detection method based on only TMB and H_2O_2 (0.39 μM).[41] The LoD of our method is lower than the concentration of iodine in the rainwater and soil samples near the Fukushima Daiichi nuclear power plant in the years 2017[57] and 2012,[58] respectively, making the method suitable for detecting I^- in a real nuclear wastewater environment.

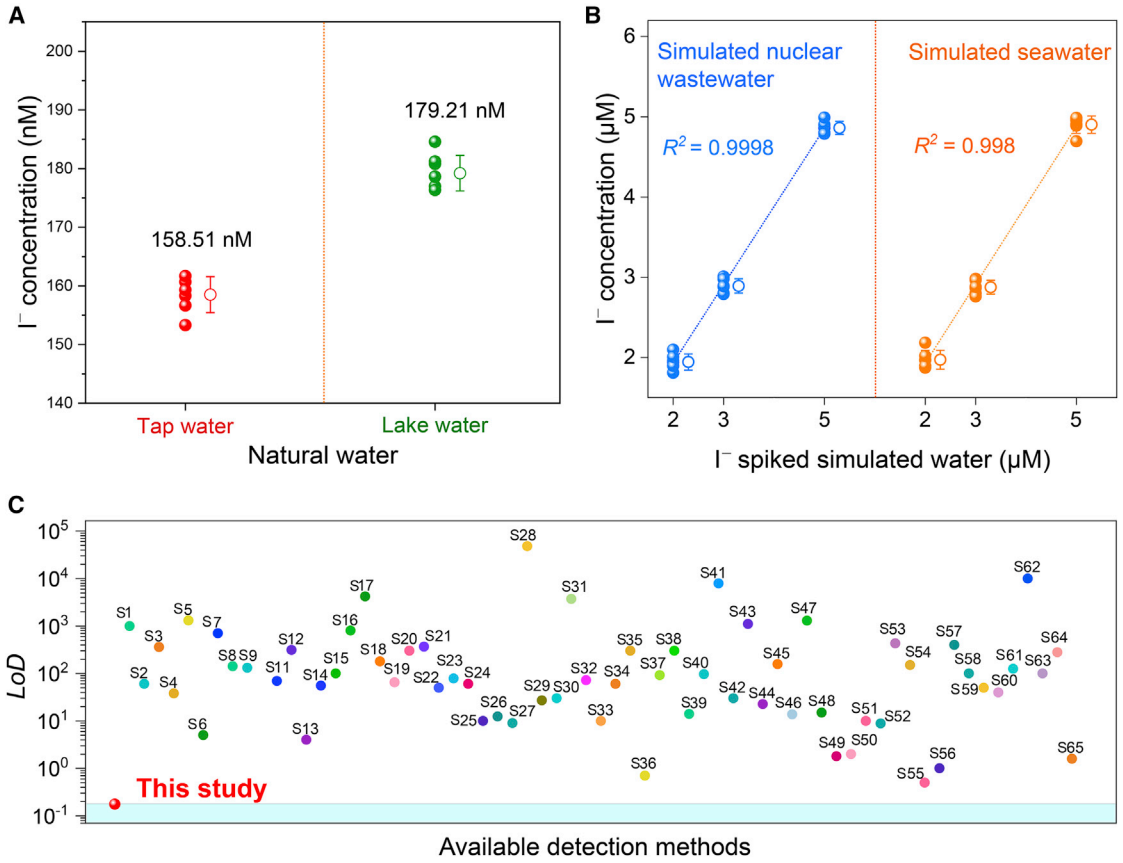

Figure 4. Practical detection of I^- in diverse aqueous environments

(A) Concentrations of I^- in tap and lake water detected using the designed method. Mean values and standard errors are shown (n = 6).

(B) Iodine ions detection in simulated nuclear wastewater and simulated seawater. The correlation between the detected and the spiked concentrations was analyzed. Mean values and standard errors are shown (n = 6).

(C) Comparison of the LoDs of our method with other methods summarized in Table S4. The corresponding references to S1 to S65 are provided in the supplemental information.

Detection specificity

Detection specificity is critical for the accurate detection of the target substance. Based on the wide existence of these ions in aqueous environments, 24 cations and 16 anions were chosen for the specificity assay. Except for I^-, the other tested ions did not change the color of the solution (Figure S11). Furthermore, these interfering ions caused rare influence on the absorbance at approximately 446 nm, indicating that the oxidation of TMB relies only on I^-. It is noteworthy that, even by coexisting with 10 times excess concentration, these 40 interfering ions only showed rare influence on the ΔA caused by I^- (Figure S12). Even by coexisting with all above 40 interfering ions, the ΔA value only decreased by 6.47%, demonstrating the ultra-high specificity of this method (Figure S13).

Practical applicability

Tap and lake waters were used to determine the applicability of our detection method. The water samples were adjusted to pH 5, and the concentrations of I^- were tested using the proposed method after suitable dilutions. The average I^- concentrations detected in tap and lake water were 158.51 and 179.21 nM, respectively (Figure 4A). The relative standard deviations (RSDs) of the detected I^- concentrations were all less than 3.05%, proving the reliability of this detection method

(Table S1). Furthermore, simulated nuclear wastewater[59] and simulated seawater[60] were spiked with different concentrations of I^- (that is, 2,000, 3,000, and 5,000 nM) (Table S2), and the concentrations of I^- were measured using this method after suitable dilution (Figure 4B). The measured I^- concentrations were very close to the spiked concentrations, and the RSDs were all less than 5.17% (Table S3), indicating the suitability of this method for detecting I^- in practical environments.

In conclusion, a Zr(IV)-based ultrasensitive and highly specific detection method for aqueous I^- was designed. In this method, Zr(IV) promotes the generation of I_2 from I^- to trigger the oxidation of TMB in the presence of H_2O_2. Furthermore, Zr(IV) directly oxidizes I^- and indirectly oxidizes I^- by boosting the generation of •OH from H_2O_2, thereby significantly enhancing the chromogenic efficiency of TMB for high-sensitivity detection of I^-. The designed method has an ultralow LoD of 0.176 nM, which is among the best available methods for I^- detection and even lower than the concentration of I^- in the radioactive pollutants near the Fukushima Daiichi nuclear power plant (Figure 4C; Table S4). Compared with the detection method based merely on TMB and H_2O_2, the LoD of this method is 2,200 times lower. Benefiting from the specific oxidation ability of I_2 to TMB, our detection method also showed ultrahigh specificity and can resist the interference of 40 interfering ions. Moreover, this detection method exhibited high practical application potential because of its excellent reliability in simulated nuclear wastewater and simulated seawater. Owing to its ultrahigh specificity and sensitivity as well as outstanding reliability, our detection method can be applied for detecting I^- in diverse environments, including nuclear wastewater, which would protect human beings from the hazard of radioactive pollution.

EXPERIMENTAL PROCEDURES

Resource availability

Lead contact

Further information and requests for resources should be directed to and will be fulfilled by the lead contact, Ning Wang (wangn02@foxmail.com).

Materials availability

This study did not generate new unique reagents.

Supplemental experimental procedures

The supplemental experimental procedures, including materials, characterization of the detection mechanism, optimization of the detection method, preparation of samples for mechanism analysis, and determination of the practical application of this method, can be found in the supplemental information.

Data and code availability

The datasets generated in this study are available from the lead contact upon reasonable request.

SUPPLEMENTAL INFORMATION

Supplemental information can be found online at https://doi.org/10.1016/j.xcrp.2022.101143.

ACKNOWLEDGMENTS

This work was supported by the Hainan Science and Technology Major Project (ZDKJ2019013 and ZDKJ2020011), the National Natural Science Foundation of

China (nos. 41966009, U1967213, and U2167220), and the Innovation Platform for Academicians of Hainan Province (HD-YSZX-202007 and HD-YSZX-202008).

AUTHOR CONTRIBUTIONS

Y.Y., N.W., and T.F. conceived the idea and designed the research. T.F., X.C., S.Z., M.C., L.F., S.S., H.W., and T.L. conducted the characterizations and reaction tests. T.F., Y.Y., N.W., A.P., L.H., R.S., and B.H. contributed to the discussion and preparation of the manuscript. All authors have given approval to the final version of the manuscript.

DECLARATION OF INTERESTS

The authors declare no competing interest.

Received: August 31, 2022
Revised: October 3, 2022
Accepted: October 14, 2022
Published: November 4, 2022

REFERENCES

1. Zhang, S., Li, H., and Wang, S. (2020). Construction of an ion pathway boosts uranium extraction from seawater. Chem *6*, 1504–1505. https://doi.org/10.1016/j.chempr.2020.06.023.

2. Xie, Y., Chen, C., Ren, X., Wang, X., Wang, H., and Wang, X. (2019). Emerging natural and tailored materials for uranium-contaminated water treatment and environmental remediation. Prog. Mater. Sci. *103*, 180–234. https://doi.org/10.1016/j.pmatsci.2019.01.005.

3. Sun, Q., Aguila, B., Song, Y., and Ma, S. (2020). Tailored porous organic polymers for task-specific water purification. Acc. Chem. Res. *53*, 812–821. https://doi.org/10.1021/acs.accounts.0c00007.

4. Xu, Y., Zhang, H., Liu, Q., Liu, J., Chen, R., Yu, J., Zhu, J., Li, R., and Wang, J. (2021). Surface hybridization of π-conjugate structure cyclized polyacrylonitrile and radial microsphere shaped TiO_2 for reducing U(VI) to U(IV). J. Hazard Mater. *416*, 125812. https://doi.org/10.1016/j.jhazmat.2021.125812.

5. Li, H., and Wang, S. (2021). Reaction: semiconducting MOFs offer new strategy for uranium extraction from seawater. Chem *7*, 279–280. https://doi.org/10.1016/j.chempr.2021.01.013.

6. Zhang, Y., Cai, Y., Zhang, S., Gao, F., Lv, Z., Fang, M., Zhao, P., Tan, X., Hu, B., Kong, M., and Wang, X. (2022). Super-efficient extraction of U(VI) by the dual-functional sodium vanadate ($Na_2V_6O_{16}·2H_2O$) nanobelts. Chem. Eng. J. *446*, 137230. https://doi.org/10.1016/j.cej.2022.137230.

7. Wang, Z., Liu, H., Lei, Z., Huang, L., Wu, T., Liu, S., Ye, G., Lu, Y., and Wang, X. (2020). Graphene aerogel for photocatalysis-assist uranium elimination under visible light and air atmosphere. Chem. Eng. J. *402*, 126256. https://doi.org/10.1016/j.cej.2020.126256.

8. Zhang, H., Liu, W., Li, A., Zhang, D., Li, X., Zhai, F., Chen, L., Chen, L., Wang, Y., and Wang, S. (2019). Three mechanisms in one material: uranium capture by a polyoxometalate–organic framework through combined complexation, chemical reduction, and photocatalytic reduction. Angew. Chem. Int. Ed. Engl. *58*, 16110–16114. https://doi.org/10.1002/anie.201909718.

9. Xiao, C., Khayambashi, A., and Wang, S. (2019). Separation and remediation of $^{99}TcO_4^-$ from aqueous solutions. Chem. Mater. *31*, 3863–3877. https://doi.org/10.1021/acs.chemmater.9b00329.

10. Morton, L.M., Karyadi, D.M., Stewart, C., Bogdanova, T.I., Dawson, E.T., Steinberg, M.K., Dai, J., Hartley, S.W., Schonfeld, S.J., Sampson, J.N., et al. (2021). Radiation-related genomic profile of papillary thyroid carcinoma after the Chernobyl accident. Science *372*, 2538. https://doi.org/10.1126/science.abg2538.

11. Feng, L., Yuan, Y., Yan, B., Feng, T., Jian, Y., Zhang, J., Sun, W., Lin, K., Luo, G., and Wang, N. (2022). Halogen hydrogen-bonded organic framework (XHOF) constructed by singlet open-shell diradical for efficient photoreduction of U(VI). Nat. Commun. *13*, 1389. https://doi.org/10.1038/s41467-022-29107-9.

12. Sun, Q., Aguila, B., Perman, J., Ivanov, A.S., Bryantsev, V.S., Earl, L.D., Abney, C.W., Wojtas, L., and Ma, S. (2018). Bio-inspired nano-traps for uranium extraction from seawater and recovery from nuclear waste. Nat. Commun. *9*, 1644. https://doi.org/10.1038/s41467-018-04032-y.

13. Li, J., Wang, X., Zhao, G., Chen, C., Chai, Z., Alsaedi, A., Hayat, T., and Wang, X. (2018). Metal–organic framework-based materials: superior adsorbents for the capture of toxic and radioactive metal ions. Chem. Soc. Rev. *47*, 2322–2356. https://doi.org/10.1039/C7CS00543A.

14. Sun, Q., Aguila, B., and Ma, S. (2019). Opportunities of porous organic polymers for radionuclide sequestration. Trends Chem. *1*, 292–303. https://doi.org/10.1016/j.trechm.2019.02.010.

15. Sun, Q., Song, Y., Aguila, B., Ivanov, A.S., Bryantsev, V.S., and Ma, S. (2021). Spatial engineering direct cooperativity between binding sites for uranium sequestration. Adv. Sci. *8*, 2001573. https://doi.org/10.1002/advs.202001573.

16. Kosaka, K., Asami, M., Kobashigawa, N., Ohkubo, K., Terada, H., Kishida, N., and Akiba, M. (2012). Removal of radioactive iodine and cesium in water purification processes after an explosion at a nuclear power plant due to the Great East Japan Earthquake. Water Res. *46*, 4397–4404. https://doi.org/10.1016/j.watres.2012.05.055.

17. Chen, J., Gu, A., Djam Miensah, E., Liu, Y., Wang, P., Mao, P., Gong, C., Jiao, Y., Chen, K., Zhang, Z., and Yang, Y. (2021). Core-shell ZnO@Cu_2O encapsulated Ag NPs nanocomposites for photooxidation-adsorption of iodide anions under visible light. Sep. Purif. Technol. *262*, 118328. https://doi.org/10.1016/j.seppur.2021.118328.

18. Chapman, K.W., Chupas, P.J., and Nenoff, T.M. (2010). Radioactive iodine capture in silver-containing mordenites through nanoscale silver iodide formation. J. Am. Chem. Soc. *132*, 8897–8899. https://doi.org/10.1021/ja103110y.

19. Chen, J., Gu, A., Miensah, E.D., Liu, Y., Wang, P., Mao, P., Gong, C., Jiao, Y., Chen, K., and Yang, Y. (2021). Cu-Zn bimetal ZIFs derived nanowhisker zero-valent copper decorated ZnO nanocomposites induced oxygen activation for high-efficiency iodide elimination. J. Hazard Mater. *416*, 126097. https://doi.org/10.1016/j.jhazmat.2021.126097.

20. Yang, D., Sarina, S., Zhu, H., Liu, H., Zheng, Z., Xie, M., Smith, S.V., and Komarneni, S. (2011). Capture of radioactive cesium and iodide ions from water by using titanate nanofibers and nanotubes. Angew. Chem. Int. Ed. Engl. *50*,

10594–10598. https://doi.org/10.1002/anie.201103286.

21. Yang, B., Yin, K., Li, X., and Liu, Z. (2022). Graph model under grey and unknown preferences for resolving conflicts on discharging Fukushima nuclear wastewater into the ocean. J. Clean. Prod. *332*, 130019. https://doi.org/10.1016/j.jclepro.2021.130019.

22. Lei, Y., Zhang, G., Zhang, Q., Yu, L., Li, H., Yu, H., and He, Y. (2021). Visualization of gaseous iodine adsorption on single zeolitic imidazolate framework-90 particles. Nat. Commun. *12*, 4483. https://doi.org/10.1038/s41467-021-24830-1.

23. Schwehr, K.A., and Santschi, P.H. (2003). Sensitive determination of iodine species, including organo-iodine, for freshwater and seawater samples using high performance liquid chromatography and spectrophotometric detection. Anal. Chim. Acta X. *482*, 59–71. https://doi.org/10.1016/S0003-2670(03)00197-1.

24. Sun, J., Wang, D., Cheng, H., Liu, J., Wang, Y., and Xu, Z. (2015). Use of ion-pairing reagent for improving iodine speciation analysis in seaweed by pressure-driven capillary electrophoresis and ultraviolet detection. J. Chromatogr. A *1379*, 112–117. https://doi.org/10.1016/j.chroma.2014.12.056.

25. Li, Y.J., Tseng, Y.T., Unnikrishnan, B., and Huang, C.C. (2013). Gold-nanoparticles-modified cellulose membrane coupled with laser desorption/ionization mass spectrometry for detection of iodide in urine. ACS Appl. Mater. Interfaces *5*, 9161–9166. https://doi.org/10.1021/am4025824.

26. Rong, Z., Wang, C., Wang, J., Wang, D., Xiao, R., and Wang, S. (2016). Magnetic immunoassay for cancer biomarker detection based on surface-enhanced resonance Raman scattering from coupled plasmonic nanostructures. Biosens. Bioelectron. *84*, 15–21. https://doi.org/10.1016/j.bios.2016.04.006.

27. Lei, Y., Yu, L., Huang, W., Yu, H., and He, Y. (2020). Visual detection of iodide ion by total internal reflection of single oxygen microbubble. ACS Sustain. Chem. Eng. *8*, 17322–17326. https://doi.org/10.1021/acssuschemeng.0c07397.

28. Liu, W., Dai, X., Bai, Z., Wang, Y., Yang, Z., Zhang, L., Xu, L., Chen, L., Li, Y., Gui, D., et al. (2017). Highly sensitive and selective uranium detection in natural water systems using a luminescent mesoporous metal–organic framework equipped with abundant Lewis basic sites: a combined batch, X-ray absorption spectroscopy, and first principles simulation investigation. Environ. Sci. Technol. *51*, 3911–3921. https://doi.org/10.1021/acs.est.6b06305.

29. Xu, D., Chen, L., Dai, X., Li, B., Wang, Y., Liu, W., Li, J., Tao, Y., Wang, Y., Liu, Y., et al. (2020). A porous aromatic framework functionalized with luminescent iridium(III) organometallic complexes for turn-on sensing of $^{99}TcO_4^-$. ACS Appl. Mater. Interfaces *12*, 15288–15297. https://doi.org/10.1021/acsami.0c01929.

30. Liu, J., Lin, Q., Zhang, Y.-M., and Wei, T.-B. (2014). A reversible and highly selective fluorescent probe for monitoring Hg^{2+} and iodide in aqueous solution. Sensor. Actuator. B Chem. *196*, 619–623. https://doi.org/10.1016/j.snb.2014.02.062.

31. Fukushima, Y., and Aikawa, S. (2021). Colorimetric detection of iodide ion by a nuclear fast red-based Hg^{2+} complex in aqueous media. Tetrahedron Lett. *67*, 152877. https://doi.org/10.1016/j.tetlet.2021.152877.

32. Masih, D., Aly, S.M., Alarousu, E., and Mohammed, O.F. (2015). Photoinduced triplet-state electron transfer of platinum porphyrin: a one-step direct method for sensing iodide with an unprecedented detection limit. J. Mater. Chem. *3*, 6733–6738. https://doi.org/10.1039/C4TA07033J.

33. Dorazco-Gonzalez, A. (2014). Chemosensing of chloride based on a luminescent platinum(II) NCN pincer complex in aqueous media. Organometallics *33*, 868–875. https://doi.org/10.1021/om4007054.

34. Tang, X., Yu, H., Bui, B., Wang, L., Xing, C., Wang, S., Chen, M., Hu, Z., and Chen, W. (2021). Nitrogen-doped fluorescence carbon dots as multi-mechanism detection for iodide and curcumin in biological and food samples. Bioact. Mater. *6*, 1541–1554. https://doi.org/10.1016/j.bioactmat.2020.11.006.

35. Ho, H.A., and Leclerc, M. (2003). New colorimetric and fluorometric chemosensor based on a cationic polythiophene derivative for iodide-specific detection. J. Am. Chem. Soc. *125*, 4412–4413. https://doi.org/10.1021/ja028765p.

36. Bao, Z.l., Zhong, H., Li, X.R., Zhang, A.R., Liu, Y.X., Chen, P., Cheng, Z.P., and Qian, H.Y. (2021). Core-shell Au@Ag nanoparticles on carboxylated graphene for simultaneous electrochemical sensing of iodide and nitrite. Sensor. Actuator. B Chem. *345*, 130319. https://doi.org/10.1016/j.snb.2021.130319.

37. Liu, W., Dai, X., Wang, Y., Song, L., Zhang, L., Zhang, D., Xie, J., Chen, L., Diwu, J., Wang, J., et al. (2019). Ratiometric monitoring of thorium contamination in natural water using a dual-emission luminescent europium organic framework. Environ. Sci. Technol. *53*, 332–341. https://doi.org/10.1021/acs.est.8b04728.

38. Jian, T., Zhou, Y., Wang, P., Yang, W., Mu, P., Zhang, X., Zhang, X., and Chen, C.L. (2022). Highly stable and tunable peptoid/hemin enzymatic mimetics with natural peroxidase-like activities. Nat. Commun. *13*, 3025. https://doi.org/10.1038/s41467-022-30285-9.

39. Pu, Y., Wu, W., Zhou, B., Xiang, H., Yu, J., Yin, H., Zhang, Y., Du, D., Chen, Y., and Xu, H. (2022). Starvation therapy enabled "switch-on" NIR-II photothermal nanoagent for synergistic in situ photothermal immunotherapy. Nano Today *44*, 101461. https://doi.org/10.1016/j.nantod.2022.101461.

40. Zhu, D., Zhang, M., Pu, L., Gai, P., and Li, F. (2022). Nitrogen-enriched conjugated polymer enabled metal-free carbon nanozymes with efficient oxidase-like activity. Small *18*, 2104993. https://doi.org/10.1002/smll.202104993.

41. Rendl, J., Bier, D., Groh, T., and Reiners, C. (1998). Rapid urinary iodide test. J. Clin. Endocrinol. Metab. *83*, 1007–1012. https://doi.org/10.1210/jcem.83.3.4633.

42. Li, F., France, L.J., Cai, Z., Li, Y., Liu, S., Lou, H., Long, J., and Li, X. (2017). Catalytic transfer hydrogenation of butyl levulinate to γ-valerolactone over zirconium phosphates with adjustable Lewis and Brønsted acid sites. Appl. Catal. B Environ. *214*, 67–77. https://doi.org/10.1016/j.apcatb.2017.05.013.

43. Gong, W., Chen, X., Jiang, H., Chu, D., Cui, Y., and Liu, Y. (2019). Highly stable Zr(IV)-Based metal–organic frameworks with chiral phosphoric acids for catalytic asymmetric tandem reactions. J. Am. Chem. Soc. *141*, 7498–7508. https://doi.org/10.1021/jacs.9b02294.

44. Lu, Z., Liu, J., Zhang, X., Liao, Y., Wang, R., Zhang, K., Lyu, J., Farha, O.K., and Hupp, J.T. (2020). Node-accessible zirconium MOFs. J. Am. Chem. Soc. *142*, 21110–21121. https://doi.org/10.1021/jacs.0c09782.

45. Tang, J., Li, P., Islamoglu, T., Li, S., Zhang, X., Son, F.A., Chen, Z., Mian, M.R., Lee, S.-J., Wu, J., and Farha, O.K. (2021). Micropore environment regulation of zirconium MOFs for instantaneous hydrolysis of an organophosphorus chemical. Cell Reports Physical Science *2*, 100612. https://doi.org/10.1016/j.xcrp.2021.100612.

46. Li, C., Li, A., Luo, Z., Zhang, J., Chang, X., Huang, Z., Wang, T., and Gong, J. (2017). Surviving high-temperature calcination: ZrO_2-induced hematite nanotubes for photoelectrochemical water oxidation. Angew. Chem. Int. Ed. Engl. *56*, 4150–4155. https://doi.org/10.1002/anie.201611330.

47. Ma, M., Hou, P., Cao, J., Liu, H., Yan, X., Xu, X., Yue, H., Tian, G., and Feng, S. (2019). Simple basic zirconium carbonate: low temperature catalysis for hydrogen transfer of biomass-derived carboxides. Green Chem. *21*, 5969–5979. https://doi.org/10.1039/C9GC03033F.

48. Zheng, T., Yang, Z., Gui, D., Liu, Z., Wang, X., Dai, X., Liu, S., Zhang, L., Gao, Y., Chen, L., et al. (2017). Overcoming the crystallization and designability issues in the ultrastable zirconium phosphonate framework system. Nat. Commun. *8*, 15369. https://doi.org/10.1038/ncomms15369.

49. Qin, J., Long, Y., Sun, F., Zhou, P.P., Wang, W.D., Luo, N., and Ma, J. (2022). $Zr(OH)_4$-Catalyzed controllable selective oxidation of anilines to azoxybenzenes, azobenzenes and nitrosobenzenes. Angew. Chem. Int. Ed. Engl. *61*, 202112907. https://doi.org/10.1002/anie.202112907.

50. Greenwood, N., and Earnshaw, A. (1997). Chapter 21 Titanium, Zirconium and Hafnium. Chemistry of the Elements (Oxford, Butterworth-Heinemann), pp. 954–975. https://doi.org/10.1016/B978-0-7506-3365-9.50027-4.

51. Lopes, N.I.A., Henrique Jardim Freire, N., Resende, P.D., Santos, L.A., and Buono, V.T.L. (2018). Electrochemical deposition and characterization of ZrO_2 ceramic nanocoatings on superelastic NiTi alloy. Appl. Surf. Sci. *450*, 21–30. https://doi.org/10.1016/j.apsusc.2018.04.154.

52. Ariyarathna, I.R., and Miliordos, E. (2020). Ab initio investigation of the ground and excited states of ZrO^+ and NbO^+. J. Quant. Spectrosc. Radiat. Transf. *255*, 107265. https://doi.org/10.1016/j.jqsrt.2020.107265.

53. Xie, L., Zheng, Z., Lin, Q., Zhou, H., Ji, X., Sessler, J.L., and Wang, H. (2022). Calix [4] pyrrole-based crosslinked polymer networks for highly effective iodine adsorption from water. Angew. Chem. Int. Ed. Engl. *61*, e202113724. https://doi.org/10.1002/anie.202113724.

54. Zhang, X., Yang, Q., Lang, Y., Jiang, X., and Wu, P. (2020). Rationale of 3, 3′, 5, 5′-tetramethylbenzidine as the chromogenic substrate in colorimetric analysis. Anal. Chem. *92*, 12400–12406. https://doi.org/10.1021/acs.analchem.0c02149.

55. Liu, M., Zhang, Y., Chen, Y., Xie, Q., and Yao, S. (2008). EQCM and in situ FTIR spectroelectrochemistry study on the electrochemical oxidation of TMB and the effect of large-sized anions. J. Electroanal. Chem. *622*, 184–192. https://doi.org/10.1016/j.jelechem.2008.06.002.

56. Feng, T., Yuan, Y., Zhao, S., Feng, L., Yan, B., Cao, M., Zhang, J., Sun, W., Lin, K., and Wang, N. (2022). Ultrasensitive detection of aqueous uranyl based on uranyl-triggered protein photocleavage. Angew. Chem. Int. Ed. Engl. *61*, 202115886. https://doi.org/10.1002/anie.202115886.

57. Matsumura, M., Sasa, K., Matsunaka, T., Sueki, K., Takahashi, T., and Matsuzaki, H. (2018). Temporal variation of iodine-129 in rainwater at tsukuba before and after the Fukushima Daiichi nuclear power plant accident. Geochem. J. *52*, 155–162. https://doi.org/10.2343/geochemj.2.0505.

58. Miyake, Y., Matsuzaki, H., Fujiwara, T., Saito, T., Yamagata, T., Honda, M., and Muramatsu, Y. (2012). Isotopic ratio of radioactive iodine released from Fukushima Daiichi NPP accident. Geochem. J. *46*, 327–333. https://doi.org/10.2343/geochemj.2.0210.

59. Zhang, J., Feng, L., Jian, Y., Luo, G., Wang, M., Hu, B., Liu, T., Li, J., Yuan, Y., and Wang, N. (2022). Interlayer spacing adjusted zirconium phosphate with 2D ion channels for highly efficient removal of uranium contamination in radioactive effluent. Chem. Eng. J. *429*, 132265. https://doi.org/10.1016/j.cej.2021.132265.

60. Sun, W., Feng, L., Zhang, J., Lin, K., Wang, H., Yan, B., Feng, T., Cao, M., Liu, T., Yuan, Y., and Wang, N. (2022). Amidoxime group-anchored single cobalt atoms for anti-biofouling during uranium extraction from seawater. Adv. Sci. *9*, 2105008. https://doi.org/10.1002/advs.202105008.